

# Electron Beam Induced Damage of NaNO<sub>3</sub> Single Crystals: An Energy, Temperature, and Quantum State Resolved Study

N. G. Petrik,<sup>†</sup> K. Knutsen, E. Paparazzo,<sup>‡</sup> S. Lea, D. M. Camaioni, and T. M. Orlando<sup>§</sup>

W. R. Wiley Environmental Molecular Sciences Laboratory, Pacific Northwest National Laboratory, MS K8-88, P.O. Box 999, Richland, Washington 99352

Received: September 16, 1999

Electron beam induced damage of NaNO<sub>3</sub> single crystals is examined using laser resonance enhanced multiphoton ionization detection of the neutral desorption products, post-irradiation temperature-programmed desorption (TPD), secondary electron emission microscopy (SEEM), and Auger electron spectroscopy (AES). The damage initially involves destruction of the nitrate group and production of O (<sup>3</sup>P<sub>J</sub>) and NO (<sup>2</sup>Π) fragments with nonthermal energy distributions. Specifically, the O (<sup>3</sup>P<sub>J</sub>) *J* state distribution measured at 100 eV incident electron energy is 5:1.5:0.25 for *J* = 2:1:0, the NO (<sup>2</sup>Π) vibrational state distribution is 1:0.56:0.35:0.40:0.23 for *v* = 0:1:2:3:4, and the NO (<sup>2</sup>Π<sub>1/2,3/2</sub>) rotational distribution has a high population of the upper (<sup>2</sup>Π<sub>3/2</sub>) spin-orbit component. Production and desorption of these nonthermal fragments are dominated by the decay of {NO<sub>3</sub><sup>−</sup>}\*. At higher electron fluences, thermalized NO, O<sub>2</sub>, and NO<sub>2</sub> are also produced and released, though the NO<sub>2</sub> is a minor product. We suggest that the formation and desorption of thermalized NO and O<sub>2</sub> both involve NO<sub>2</sub><sup>−</sup> defect states and unimolecular dissociation of NO<sub>3</sub>\*. This is supported by the observation that the NO and O<sub>2</sub> yields have the same temperature dependence which is well described by the sum of two Maxwell-Boltzmann type equations with activation energies of 0.16 ± 0.03 and 0.010 ± 0.004 eV. O<sub>2</sub> gas is also released in post-irradiation thermal cycling from 110 to 440 K with peaks at ~260 and ~340 K. We associate the post-irradiation TPD of O<sub>2</sub> with reactions involving O atoms released during thermal decomposition of {NO<sub>2</sub><sup>−</sup>...O} and ONOO<sup>−</sup>. The SEEM image shows damage features, and the AES spectra indicate that the irradiated region is depleted in both nitrogen and oxygen relative to Na. The elemental composition shows Na<sub>2</sub>O as a final product of the NaNO<sub>3</sub> radiation decomposition. The 100 eV electron beam damage cross section is at least ~10<sup>−16</sup> cm<sup>2</sup>.

## I. Introduction

Sodium nitrate (NaNO<sub>3</sub>) is a wide band gap ionic material with the calcite-type rhombohedral lattice and is stable at temperatures below ~550 K. The cleavage plane is along the 1014 direction and intersects the *c* axis at an angle of 43°49'.<sup>1,2</sup> There is recent interest in this material since it is a good model for molecular ionic solids containing polyatomic anions. NaNO<sub>3</sub> is an important constituent of atmospheric aerosols<sup>3,4</sup> and also a major component of some high-level "mixed" (radioactive/chemical) wastes currently in underground storage tanks at some United States Department of Energy facilities.<sup>5</sup> Gases such as hydrogen, oxygen, ammonia, and nitrous oxide are produced and released at these facilities in a manner which is not easy to mitigate. As an initial step in the study of whether radiation-induced processes within porous solids or at interfaces contribute to the generation of these gases, we have performed a detailed study of electron interactions with NaNO<sub>3</sub> single crystals using tools and techniques of modern surface science.

Many previous studies on the electron, ion, X-ray, and gamma bombardment of NaNO<sub>3</sub> have shown that dissociation of the

oxyanion group is dominant and reactive scattering of the atomic and molecular fragments results in secondary chemical transformations.<sup>6–8</sup> Ionization is a dominant energy loss channel, and excitation energies above the valence to Na derived conduction band transition at ~10–11 eV produce electron-hole pairs. The holes can localize or self-trap generating NO<sub>3</sub> centers or interact with NO<sub>2</sub><sup>−</sup> defects to produce NO<sub>2</sub>.<sup>9–11</sup> The electrons can also be trapped, and the high electron affinity of NO<sub>3</sub><sup>−</sup> leads to a relatively low concentration of F-type centers in favor of NO<sub>3</sub><sup>2−</sup> electron centers at low temperatures. NO<sub>3</sub> and NO<sub>3</sub><sup>2−</sup> defects have been detected at 77 K by optical absorption and electron spin resonance techniques, and these defects recombine with electrons or holes in less than 10<sup>−6</sup> s at 300 K.<sup>12–15</sup>

Excitation energies below the valence-to-conduction band transition can also produce defects. Though the absolute threshold for defect creation in single crystals of NaNO<sub>3</sub> is not well-known, excitation of the π\* ← π band of the NO<sub>3</sub><sup>−</sup> anion near 6 eV produces NO (<sup>2</sup>Π) and O (<sup>3</sup>P<sub>J</sub>) fragments at the surface<sup>16</sup> and may also produce NO<sub>2</sub><sup>−</sup>, atomic oxygen, peroxy-nitrite ONOO<sup>−</sup> anions,<sup>17–20</sup> and a caged complex {NO<sub>2</sub><sup>−</sup>...O}<sup>21</sup> in the bulk. The escape of O atoms from the {NO<sub>3</sub><sup>−</sup>}\* produces NO<sub>2</sub><sup>−</sup> defects and involves nonactivated and thermally activated processes.<sup>22,23</sup> The latter depends significantly on the phonon density of states and free space in the crystal lattice of the nitrate salts.<sup>22–25</sup> In the bulk, escaped O atoms can combine yielding molecular oxygen or react with nitrate anions producing NO<sub>2</sub><sup>−</sup> + O<sub>2</sub>.<sup>6,7,25</sup> The {NO<sub>2</sub><sup>−</sup>...O} and ONOO<sup>−</sup> products are stable at

<sup>†</sup> Visiting Scientist from the All-Russian Project and Research Institute of Complex Power Technology "VNIPIET", 55 Dibunovsklaja St., St. Petersburg 197228, Russia.

<sup>‡</sup> Visiting Scientist from the Istituto di Struttura della Materia del CNR, Area della Ricerca di Roma-Tor Vergata, Via del Fosso del Cavaliere, 00133 Roma, Italy.

<sup>§</sup> To whom correspondence should be addressed. E-mail: Thomas.Orlando@pnl.gov. Fax: 509 376-6066.

liquid nitrogen temperature (77 K) and decompose at 220–250 K and  $\sim 360$  K, respectively, to form  $\text{NO}_3^-$  and  $\text{NO}_2^- + \text{O}$ .<sup>14,21,26</sup>

Damage and desorption studies of  $\text{NaNO}_3$  using high-energy ( $> 1$  keV) electrons,<sup>27</sup> low-energy (5–100 eV) electrons,<sup>28,29</sup> and ultraviolet photons<sup>16,30–34</sup> have been carried out. All of these studies report NO as a primary desorption product, in contrast to bulk damage studies which demonstrate  $\text{NO}_2^-$  and occluded  $\text{O}_2$  as major products above room temperature. Recently, studies also observed O ( $^3\text{P}_j$ ) fragments<sup>16,29</sup> and noted that  $\text{O}_2$  was a minor electron-stimulated desorption (ESD) product under low-energy, low-dose conditions.<sup>29</sup> Irradiation studies using higher electron energies (1–3 keV) and higher doses reported the thermally assisted delayed emission of  $\text{O}_2$  and  $\text{NO}$ .<sup>27</sup> The delayed emission was partially attributed to the dose conditions and dissociative electron attachment processes.

An energy-, temperature- and quantum state-resolved study can yield valuable information concerning the mechanisms of electron-beam induced damage of molecular solids such as  $\text{NaNO}_3$ . In this article, we present the results of such a study. We describe the experimental approaches used in section 2 and present our state-resolved ESD, temperature-dependent ESD, post-irradiation temperature-programmed desorption (TPD), secondary electron emission microscopy (SEEM), and Auger electron spectroscopy (AES) results in section 3. We discuss the dominant electronic excitations and damage mechanisms and then present a qualitative model in section 4. Finally, our overall conclusions are stated in section 5.

## II. Experiment

Solution- and melt-grown  $\text{NaNO}_3$  single crystals ( $10 \times 10 \times 2$  mm<sup>3</sup>) were cleaved along the 1014 plane and mounted on a cryogenically cooled Mo sample holder in an ultrahigh vacuum ( $1 \times 10^{-10}$  Torr) chamber. The crystals were then baked at 400 K for several days to remove adsorbed water and other contaminants such as hydrocarbons. Subsequent thermal desorption measurements indicated that surface contamination was negligible. The samples were then annealed for 2–3 h at 430 K, a temperature below the onset of an order–disorder phase transition. The sample temperature was then varied from 100 to 430 K via electron bombardment of the rear side of the Mo mounting plate utilizing a feedback controlled heated tungsten filament. Two type-K (Chromel–Alumel) thermocouples were used for the temperature measurements; the first one was welded to the Mo mounting plate, and the second one was welded to a 2 mm  $\times$  2 mm piece of Ta foil which was pressed to the outer surface of the crystal. Uncertainty in the absolute temperature measurements was  $\pm 10$  K due to the low thermal conductivity of  $\text{NaNO}_3$ . The samples were heated to 400–420 K before each ESD measurement and the electron beam position was periodically changed to minimize radiation damage of the surface.

A Kimbal Physics ELG-2 low-energy electron gun was utilized as the electron beam source. The incident energy was variable from 5 to 100 eV with a full width at a half-maximum of 0.30 eV. The pulsed beam supplied an electron fluence of  $\sim 10^9$  electrons per cm<sup>2</sup> per pulse. The electron beam pulse width was 200–250 ns for the resonance enhanced multiphoton ionization (REMPI)/time-of-flight (TOF) detection configuration, and 1–10  $\mu\text{s}$  for the quadrupole mass spectrometer (QMS) detection. The temperature-dependent yield studies were carried out under continuous electron irradiation, using an electron energy of  $100 \pm 0.5$  eV, beam current density of  $\sim 10$   $\mu\text{A}/\text{cm}^2$ , and a maximal dose of  $\sim 10^{16}$  electron/cm<sup>2</sup>. This current density

is not high enough to expect significant electron interactions with desorbed species. Since  $\text{NaNO}_3$  is an insulating material, possible sample charging problems were checked by monitoring the sample image with the electron beam. The sample images, taken as “electron beam current vs beam deflection”, showed no significant changes over the temperature range (110–420 K) studied. Charging was therefore considered to be inconsequential under the conditions utilized in this experiment.

Yields of neutral desorbates vs incident electron energy and quantum-resolved time-of-flight distributions were obtained utilizing a REMPI/TOF configuration which has been described in detail elsewhere.<sup>16</sup> Briefly, the desorbing plume was crossed by a pulsed probe laser beam which was focused to  $\sim 100$   $\mu\text{m}$  beam waist 4 mm above and parallel to the sample surface. The probe laser ionizes the neutrals via resonant multiphoton transitions and the ions are collected in the TOF mass spectrometer oriented normal to the crystal surface. The time-of-flight and thus the velocity distributions of the neutral desorbates are measured by varying the time delay between the electron beam pulse and REMPI laser pulse. The laser detection schemes utilized were 1 + 1 REMPI via the  $^2\Sigma^+$  state for NO detection<sup>35</sup> and 2 + 1 REMPI via the 3  $^3\text{P}_j$  level for O ( $^3\text{P}_j$ ) detection.<sup>36</sup> Under our experimental conditions, the typical sensitivity limits of these schemes were  $\sim 10^6$  neutrals per cm<sup>3</sup> per quantum state. Neutrals were also detected as a function of time or sample surface temperature by the QMS, which was programmed to detect 10 masses. The electron impact ionizer of the QMS was designed to prevent any electrons from escaping the ionization zone and thus surface irradiation was solely from the Kimbal Physics gun. ESD data were taken in a “beam ON–beam OFF” mode to remove any background contributions. NO and  $\text{O}_2$  desorption rates were stable during the detection time, which indicates a steady-state ESD condition. Typically, signal and background data were averaged from 300 to 400 points.

The AES spectra and SEEM images of the damaged  $\text{NaNO}_3$  single crystals were taken using a Physical Electronics 680 Auger Nanoprobe with a 1 nA beam at 3 keV. The spectra were obtained in the integral mode, and then differentiated numerically for quantitative purposes. Surface atomic percentages were derived using the elemental sensitivity factors provided by the manufacturer.<sup>37</sup>

## III. Results

**A. Energy and Quantum State Resolved ESD Measurements. *i.* NO ( $^2\Pi$ ) and O ( $^3\text{P}_j$ ) Velocity Distributions and Yields.** Quantum-resolved velocity distributions of the NO ( $^2\Pi$ ) and O ( $^3\text{P}_j$ ) products are presented in Figures 1 and 2. These distributions were obtained using an incident electron energy ( $E_i$ ) of 80 eV and REMPI/TOF detection. Specifically, the data displayed in Figure 1 were taken with the REMPI laser tuned to the ( $^2\Sigma^+ - ^2\Pi_{1/2}$ ) (0,0), (1,1), and (2,2) bandheads and on the  $N = 15$  R<sub>1</sub> transition. The data shown in Figure 2 was obtained via the  $3^3\text{P}_{j=2,1,0} \leftarrow ^3\text{P}_{j=2,1,0}$  transitions. All intensities are normalized, and the curves are displaced for the sake of comparison. Both the NO and O velocity distributions were independent of the incident electron energy and were measured at a sample temperature of  $423 \pm 5$  K. This temperature, which is below the order–disorder phase transition, reduces any effects due to the accumulation of alkali metals, defect sites, and charging.<sup>28</sup>

The velocity distributions shown in Figures 1 and 2 cannot be fit to a single Maxwell–Boltzmann distribution. However, a good fit was obtained using the sum of two such distributions:

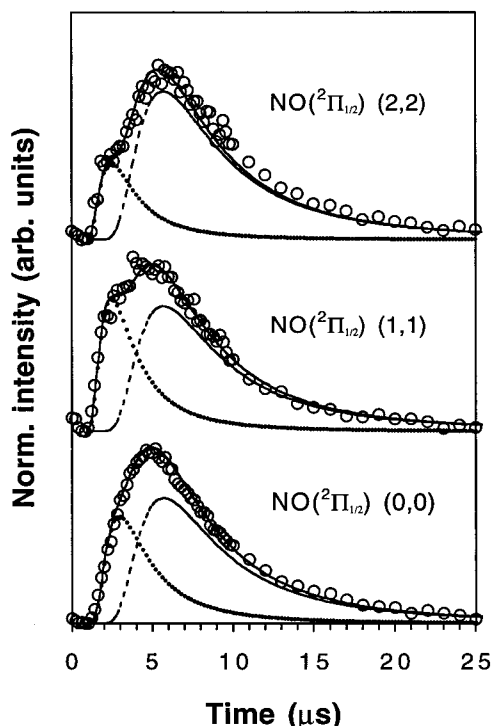


**Figure 1.** Velocity distributions for NO (<sup>2</sup>Π) obtained using resonance enhanced multiphoton ionization detection. The incident electron energy was 80 eV and the NaNO<sub>3</sub> surface temperature was held constant at 423 K. The intensities are normalized, and the curves are displaced for the sake of comparison. The solid lines are the calculated bimodal Maxwell–Boltzmann distributions with the thermal component indicated by a dashed line and the nonthermal component by a dotted line. The extracted temperatures of the nonthermal component are 1600, 2300, and 2300 K for the (0,0), (1,1), and (2,2) states, respectively.

$$I(t) = C_1 t^{-3} \exp\left(-\frac{m}{2kT_1} \frac{d^2}{t^2}\right) + C_2 t^{-3} \exp\left(-\frac{m}{2kT_2} \frac{d^2}{t^2}\right) \quad (1)$$

where  $C_1$  and  $C_2$  are proportionality constants,  $m$  is the mass of the neutral desorbate,  $k$  is Boltzmann's constant,  $d$  is the flight distance from the sample surface to the probe laser beam,  $t$  is the time delay between the electron and laser beam pulses, and  $T_1$  and  $T_2$  are effective temperatures. The " $t^{-3}$ " pre-exponential term in the eq 1 indicates a two-dimensional detection arrangement. The third dimension along the laser beam is degenerated as a result of saturation of the REMPI signal.<sup>38</sup> The form of these distributions assumes that desorption is essentially instantaneous.

The solid lines in Figures 1 and 2 are the two-temperature fits, and the dashed and dotted lines show the relative contributions of the thermal (423 K) and nonthermal components, respectively. The "hot" NO molecules represent ~30%, ~30%, and ~20% of the total NO yield and can be associated with effective temperatures of ~1600 K, ~2300 K, and ~2300 K for the (0,0), (1,1), and (2,2) vibrational states, respectively. The "hot" O yield is as high as ~30% of the total O atom yield and shows an effective temperature of ~2000 K for the <sup>3</sup>P<sub>2</sub> state (Figure 2). Velocity distributions for the  $J = 0, 1$ , and 2 states of the O (<sup>3</sup>P<sub>*J*</sub>) atom are essentially the same within the experimental error range (inset in Figure 2).

The relative NO (<sup>2</sup>Π) and O (<sup>3</sup>P<sub>*J*</sub>) yields as a function of incident electron energy are shown in Figure 3. These data were obtained with the REMPI laser delay set to the peaks of the desorbate velocity distributions such as those shown in Figures 1 and 2. The incident electron flux is constant over the energy range studied. The normalized data in Figure 3 show identical

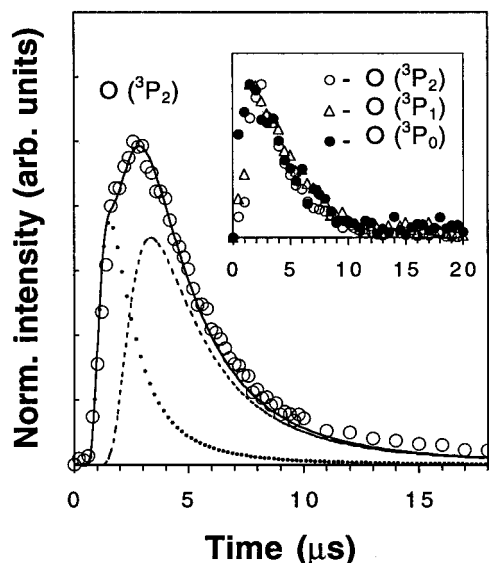


**Figure 2.** Velocity distributions for O (<sup>3</sup>P<sub>2</sub>) obtained using resonance enhanced multiphoton ionization detection. The incident electron energy was 80 eV and the NaNO<sub>3</sub> surface temperature was held constant at 423 K. The solid line is the calculated bimodal Maxwell–Boltzmann distribution with the thermal component indicated by a dashed line and the nonthermal component by a dotted line. The extracted temperature of the nonthermal component is 2000 K. Inset: velocity distributions for the  $J = 0, 1$ , and 2 states of the O (<sup>3</sup>P<sub>*J*</sub>) obtained with 80 eV electrons and a substrate temperature of 423 K. The intensities are normalized.

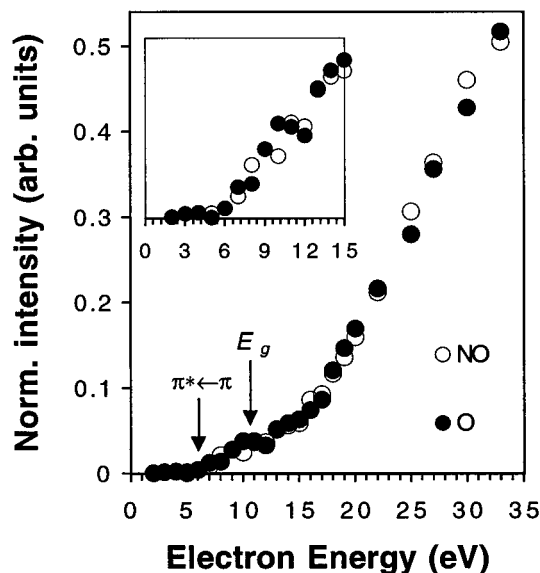


**Figure 3.** The NO (<sup>2</sup>Π) (open circles) and O (<sup>3</sup>P) (filled circles) yields as a function of incident electron energy obtained using resonance enhanced multiphoton ionization following the electron irradiation of NaNO<sub>3</sub> surface at 423 K. Electron-beam current is constant. Arrows mark the ~6 eV maximum for the  $\pi^* \leftarrow \pi$  transition of the NO<sub>3</sub><sup>-</sup> ion and ~10.5 eV band gap ( $E_g$ ) for the NaNO<sub>3</sub> crystal.

electron energy dependencies for both O and NO ESD, with two threshold energies. The arrows in Figure 3 indicate the nominal threshold energies, which are close to the  $\pi^* \leftarrow \pi$  band of the NO<sub>3</sub><sup>-</sup> ion at ~6 eV and to the valence-to-conduction band transition ( $E_g$ ) in NaNO<sub>3</sub> at ~10–11 eV.<sup>1,2</sup> We estimate an uncertainty in the threshold values of ~1–2 eV due to possible transient charging of the sample during the electron beam pulse. The yields rise significantly in the  $(1-2) \times E_g$  region, which may be associated with multiple scattering of

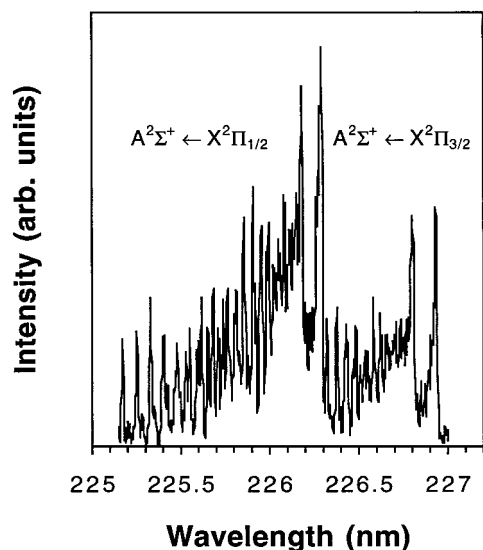


**Figure 4.** The NO rotational spectrum obtained using resonance enhanced multiphoton ionization following 100 eV electron irradiation of a  $\text{NaNO}_3$  crystal at 423 K. The spectrum displays the rotational distribution of the  $\tilde{A}, {}^2\Sigma^+(0,0) \leftarrow \tilde{X}, {}^2\Pi_{1/2,3/2}(0,0)$  transition with a nonstatistical population of the higher rotational levels and upper  $\Pi_{3/2}$  spin-orbit component.

secondary electrons and separation of electron-hole pairs.<sup>39</sup> Estimates suggest that the total desorption cross section for 100 eV ESD is larger than  $\sim 10^{-16} \text{ cm}^2$ .

ii. *NO ( ${}^2\Pi_{1/2,3/2}$ ) and O ( ${}^3P_J$ ) Internal State Distributions.* The very high detection efficiency and quantum state specificity inherent in the laser resonance enhanced multiphoton ionization techniques also allows us to probe the fine structure population of O ( ${}^3P_J$ ) and rotational and vibrational state population of the molecular NO ( ${}^2\Pi_{1/2,3/2}$ ) fragments. As an example of the latter, the measured rotational population of NO via the  $\tilde{A}, {}^2\Sigma^+(0,0) \leftarrow \tilde{X}, \Pi(0,0)$  band is displayed in Figure 4. The  $\Pi_{1/2}$  and  $\Pi_{3/2}$  band positions are indicated. This measured rotational population cannot be described in terms of a Boltzmann distribution since there is an inversion in the spin state distributions as well as unusually high population of several high- $J$  levels. We therefore do not assign any effective rotational "temperature". We have also obtained very similar rotational state distributions for the  $\nu = 1, 2, 3$ , and 4 levels. To determine the vibrational state partitioning, we have integrated the total rotational population for each vibrational level. The relative populations of the NO vibrational levels are presented in Figure 5 and correspond to 1:0.56:0.35:0.40:0.23 for  $\nu = 0:1:2:3:4$ .

To obtain the fine structure population of the O ( ${}^3P_J$ ) fragment, spectra of the  $J$  levels were measured (not shown). The spectra were obtained with a  $1 \mu\text{s}$  electron-beam pulse width and the probe laser delay set at the peak of the velocity distributions shown in Figure 2. The integrated area of the spectral lines indicates a population of 5.0:1.5:0.25 for the  $J = 2, 1, 0$  lines, respectively. This is essentially the same as the distribution measured for photon-stimulated desorption (PSD) using 6.4 eV photons<sup>16</sup> but considerably different than the 5.0:1.75:0.5 distribution expected for atoms in equilibrium with the 423 K surface temperature. We detected no O( ${}^1\text{D}$ ) fragments, in accord with previous PSD measurements at low fluence.<sup>16</sup>

**B. Temperature-Dependent ESD Measurements.** i. *100 eV Electron Beam Irradiation: NO, O<sub>2</sub>, and NO<sub>2</sub> Yields.* The molecular products released from the  $\text{NaNO}_3$  single-crystal surface under 100 eV electron beam irradiation were NO and O<sub>2</sub> with a small amount of NO<sub>2</sub>. The temperature dependence

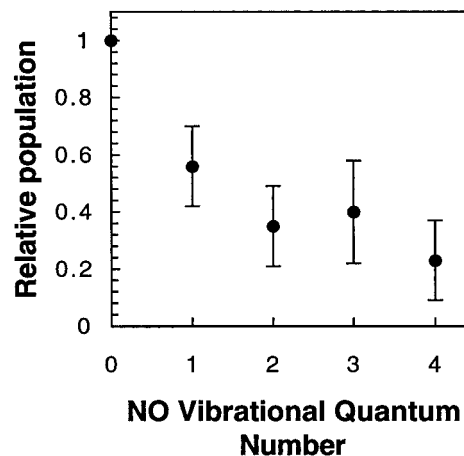


**Figure 5.** The NO vibrational state distribution showing considerable excitation out to vibrational quantum number  $\nu = 4$ . In contrast, at room temperature the relative population of the  $\nu = 4$  quantum number should be  $\sim 10^{-4}$ . Error bars represent the  $2\sigma$  statistical deviation.

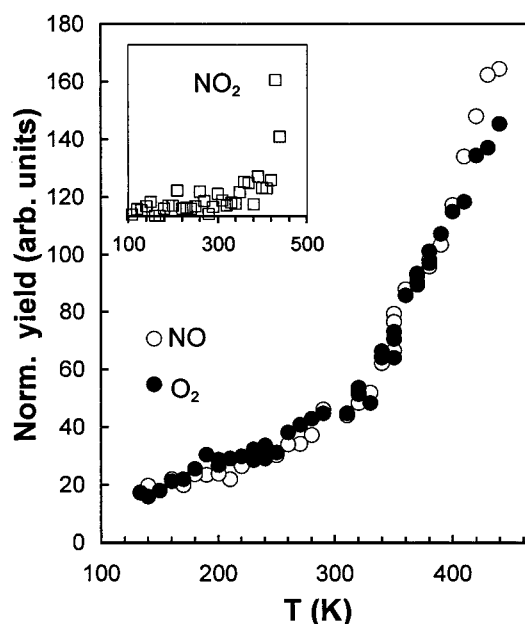


**Figure 6.** Temperature dependence of the NO (open circles), O<sub>2</sub> (filled circles), and NO<sub>2</sub> (inset, open squares) ESD yields during continuous 100 eV electron irradiation of the  $\text{NaNO}_3$  surface. The NO and O<sub>2</sub> yields are measured with the QMS and are normalized for the sake of comparison.

of the ESD yields of these molecules is shown in Figure 6 (note the NO<sub>2</sub> data is shown in the inset). The ESD of all these molecular products is thermally activated in the temperature region between 110 and 440 K and the most significant effect can be observed at temperatures above 300 K. The normalized data for the NO and O<sub>2</sub> ESD yields have essentially identical temperature dependencies within experimental error of  $\pm 15\%$ . The NO/O<sub>2</sub> ratio does not change significantly with temperature.

The data are also presented in Arrhenius coordinates in Figure 7 and can be approximated by a sum of two Maxwell-Boltzmann type equations of the form

$$I = I_{01} \exp(-E_1/kT) + I_{02} \exp(-E_2/kT) \quad (2)$$

where  $E_1$  and  $E_2$  are activation energies,  $0.16 \pm 0.03$  and  $0.010 \pm 0.004$  eV, respectively;  $I_{01}$  and  $I_{02}$  are constants. The solid line in Figure 7 is a fit using this equation. The high-temperature activation energy of NO and O<sub>2</sub> desorption is in good agreement



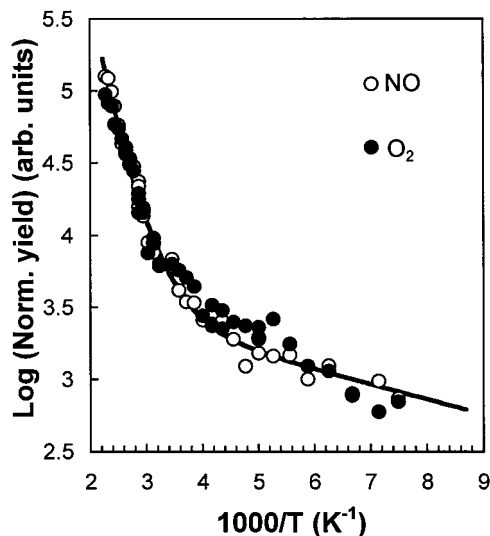


**Figure 7.** Temperature dependence of ESD yields of NO (open circles) and O<sub>2</sub> (filled circles) in Arrhenius coordinates. The NO and O<sub>2</sub> yields are normalized for the sake of comparison. The line is an approximation according to  $I = I_{01} \exp(-E_1/kT) + I_{02} \exp(-E_2/kT)$ , where  $E_1 = 0.16 \pm 0.03$  eV and  $E_2 = 0.010 \pm 0.004$  eV;  $I_{01}$  and  $I_{02}$  are the fitting coefficients.

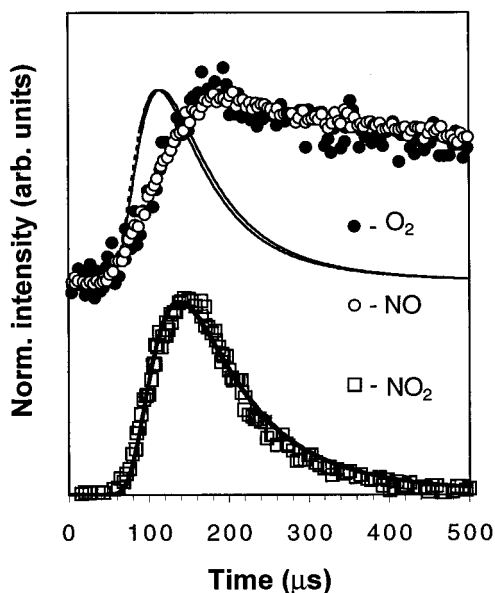


**Figure 8.** Velocity distributions for NO (open circles), O<sub>2</sub> (filled circles), and NO<sub>2</sub> (open squares) obtained using QMS detection following 100 eV electron (1  $\mu$ s pulses) irradiation of NaNO<sub>3</sub> surfaces at 423 K. The lines are 423 K Maxwell-Boltzmann distributions, calculated for the  $\sim 5$  cm flight distance between the sample and the QMS ionizer. The intensities are normalized and the curves are displaced for the sake of comparison.

with previously reported data.<sup>27</sup> The similar temperature dependencies for NO and O<sub>2</sub> ESD and the constant yield ratio may indicate that these molecules are produced via the same process and likely involve a common precursor.

*ii. NO<sub>2</sub>, NO, and O<sub>2</sub> Velocity Distributions and Desorption Kinetics.* To check the supposition of a common precursor, we measured time-dependent desorption yields under pulsed excitation and constant temperature conditions. The NO<sub>2</sub>, O<sub>2</sub>, and NO TOF distributions resulting from pulsed (1  $\mu$ s, 20 Hz, 100 eV) electron beam irradiation of NaNO<sub>3</sub> crystals held at 423 K are shown in Figure 8. The lines are the calculated 423 K Maxwell-Boltzmann distributions for O<sub>2</sub>, NO, and NO<sub>2</sub>, assuming instantaneous desorption during the electron pulse. To facilitate

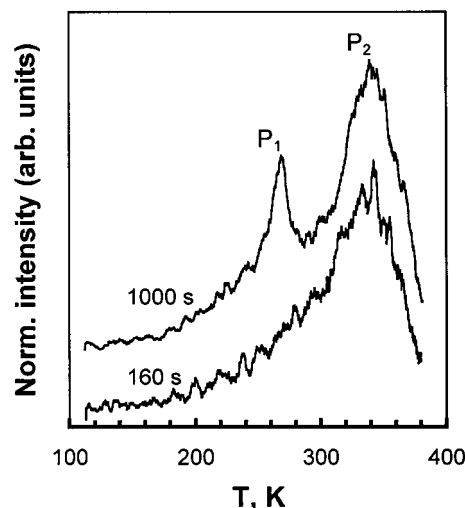


**Figure 9.** The TPD of O<sub>2</sub> from NaNO<sub>3</sub> surface irradiated at 110 K with 100 eV electrons for 160 and 1000 s which corresponds to fluences of  $\sim 1.1 \times 10^{15}$  and  $7.2 \times 10^{15}$  electron/cm<sup>2</sup>, respectively. The two main thermal desorption peaks, P<sub>1</sub> and P<sub>2</sub>, are centered at  $\sim 260$  K and  $\sim 340$  K, respectively. The intensities are normalized and the curves are displaced for the sake of comparison.

comparisons of the leading edges, all intensities are normalized. The experimental NO<sub>2</sub> velocity distribution fits the Maxwell-Boltzmann approximation for the surface temperature, indicating a prompt desorption of the thermalized NO<sub>2</sub> molecules, which is in good agreement with previously reported data.<sup>29</sup> The emission of the NO and O<sub>2</sub> is extended for several milliseconds after the electron pulse, and the delayed NO and O<sub>2</sub> emission kinetics are similar (Figure 8). The delayed emission is very consistent with previously reported 1–3 keV electron irradiation experiments,<sup>27</sup> nonresonant, high-fluence laser ablation experiments,<sup>33</sup> and 6.4 eV photon-stimulated desorption.<sup>29</sup>

*iii. Post Irradiation TPD of O<sub>2</sub>.* To obtain additional information on the long-time behavior and delayed emission, TPD of samples preirradiated at low temperature (110 K) was carried out. Figure 9 displays the TPD spectrum from samples irradiated with 100 eV electrons for 160 and 1000 s. This corresponds to doses of  $\sim 1.1 \times 10^{15}$  and  $7.2 \times 10^{15}$  electron/cm<sup>2</sup>, respectively. Molecular oxygen is the only post-irradiation TPD product observed. No significant amounts of nitrogen-containing products such as NO or NO<sub>2</sub> were detected. The O<sub>2</sub> post-irradiation desorption is characterized by a peak centered near 340 K and, after an incubation dose of  $\sim 1 \times 10^{15}$  electron/cm<sup>2</sup>, a second peak at 260 K is evident. The dose dependence of these two features can be obtained by deconvoluting the TPD curves in Figure 9 as a function of irradiation fluence. The result of this analysis is presented in Figure 10. The feature at 260 K has a clear induction period with a nonlinear dose dependence, whereas the feature at 340 K increases monotonically without an apparent dose threshold. Both features seem to reach saturation at doses greater than  $\sim 3.5 \times 10^{15}$  electron/cm<sup>2</sup>.

Control experiments indicate that oxygen does not adsorb in the molecular form on NaNO<sub>3</sub> surfaces in the temperature region between 110 and 440 K. As discussed below, the O<sub>2</sub> is likely produced and released from the bulk and cannot be due to readsorbed molecules initially released from the surface during irradiation.

**C. SEEM and Auger Analysis of the Electron Irradiated NaNO<sub>3</sub> Crystal.** Figure 11 is a SEEM image of the NaNO<sub>3</sub> surface showing the effects of electron irradiation. The square area (center portion) irradiated with 13 nA beam of 10 keV

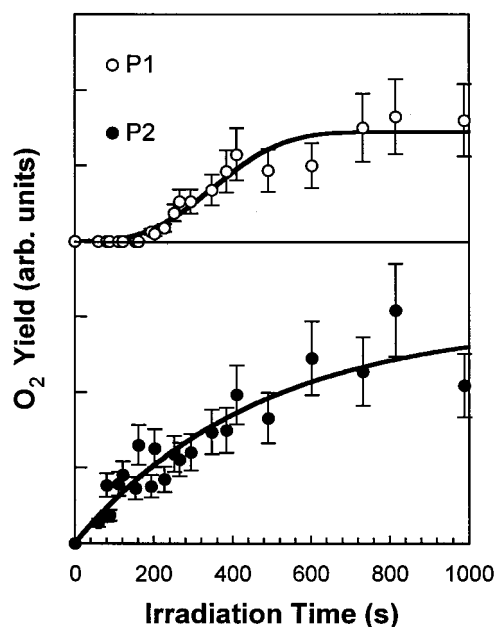


**Figure 10.** Dependence of the TPD intensity for the 260 K ( $P_1$ , open circles) and 340 K ( $P_2$ , filled circles)  $O_2$  TPD peaks as a function of electron irradiation time at 110 K. Irradiation for 1000 s is equivalent to an electron fluence of  $\sim 7.2 \times 10^{15}$  electron/cm<sup>2</sup>.

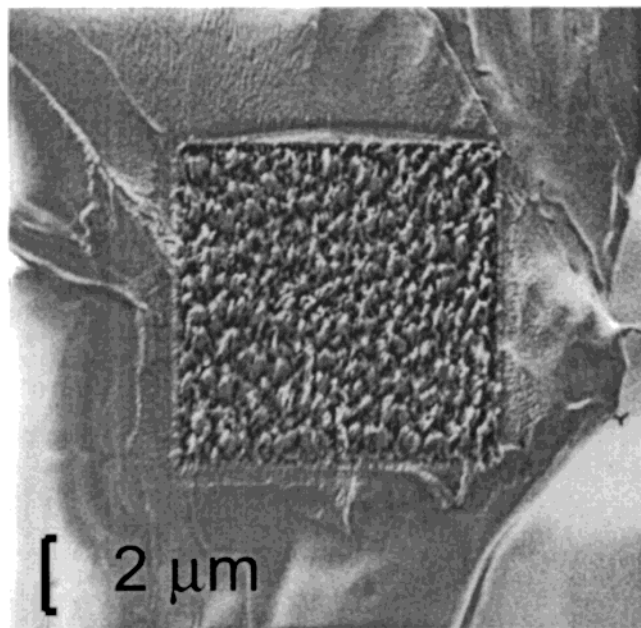


**Figure 11.** SEEM image of the  $NaNO_3$  surface, whose central area has been irradiated with a 13 nA, 10 keV electron beam for 24 h. The irradiated square area is topologically rough with a large amount of disorder and deep cone-like damage features.

electrons for 24 h is topologically rough with a large amount of disorder and deep cone-like damage features.

The AES spectrum of the damaged area is presented in Figure 12 and demonstrates the dominance of the oxygen and sodium peaks. Quantitative analysis of the spectra gives the following elemental composition of the damaged area: Na =  $64 \pm 8$  at. %; O =  $31 \pm 5$  at. %; N < 5 at. %. This clearly indicates a sizable depletion in both nitrogen and oxygen in comparison to the stoichiometric composition of  $NaNO_3$  (Na = 20 at. %, O = 60 at. %, N = 20 at. %), pointing to the presence of  $Na_2O$  as one of the main surface damage products. AES analysis identifies this oxide in the first few layers of the crystal since

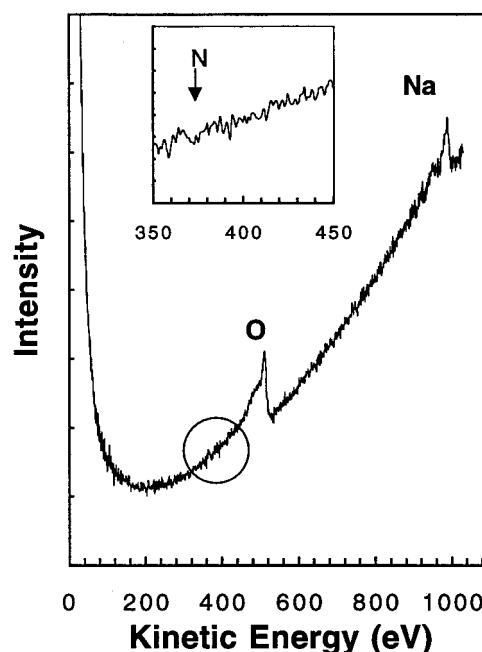


**Figure 12.** AES spectrum of the  $NaNO_3$  surface area, damaged after 10 keV electron irradiation (see Figure 11). The spectrum is taken in the integral mode and the extracted elemental composition of the damaged area is: N, <5 at. %; O,  $31 \pm 5$  at. %; Na,  $64 \pm 8$  at. %.

the inelastic mean free paths of the detected electrons are 2.4, 1.2, and 1.5 nm for the Na, N and O peaks, respectively.<sup>40</sup>

#### IV. Discussion

We have observed the *prompt* production of two translationally hot fragments during low-energy electron bombardment of  $NaNO_3$ :  $O(^3P)$  and  $NO(^2\Pi)$ . The latter is also vibrationally and rotationally excited. *Prompt* emission of  $NO_2$  and *delayed* emission of  $O_2$  and  $NO$  are also detected during electron beam irradiation of  $NaNO_3$ . The delayed  $NO$  and  $O_2$  emissions have identical kinetics and exhibit the same temperature dependencies, indicating involvement of a common precursor. In addition, release of  $O_2$  at 260 and 340 K is observed in post-irradiation thermal desorption studies. Finally, SEEM and AES show that the damaged region lacks N and O in accord with damage of the nitrate groups. To explain these collective observations, we discuss (i) prompt emission, initial excitations, and damage mechanisms, (ii) delayed emission, precursor formation, and unimolecular dissociation, and (iii) post-irradiation thermal-stimulated desorption and decomposition of the radiation induced defects.

**A. Prompt Emission, Initial Excitations, and Damage Mechanisms.** The primary energy loss channels involved in high-energy electron bombardment of materials are ionization and electronic excitation. At the energies used in this study, ionization can involve direct removal of electrons from deep and shallow core levels and/or valence bands. Holes produced via core level excitations can decay via Auger processes and cascading events, which lead to production of electron-hole pairs.<sup>39</sup> Since the electronic excitation cross section for electron impact is inversely proportional to the excitation energy,<sup>39</sup> the number of valence band holes is significantly larger than the number of core holes. The major direct excitation detected in the  $NaNO_3$  crystals is a single-center molecular exciton with absorption near 6 eV.<sup>1,2</sup>

Figures 13 and 14 illustrate several of the excitations and reaction pathways, which can occur due to electron irradiation

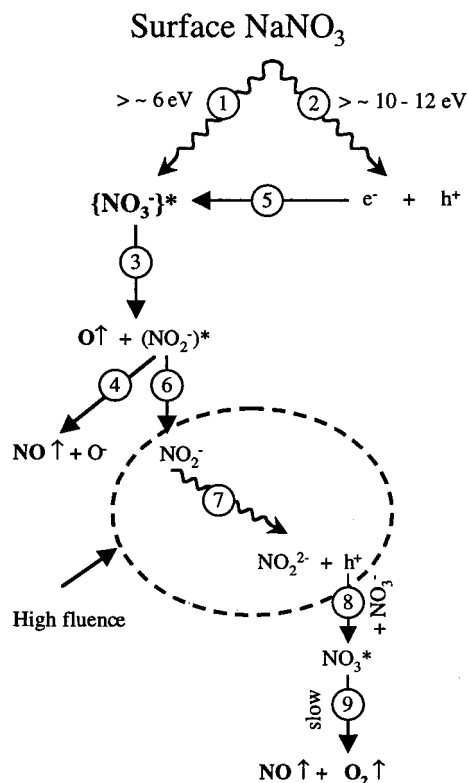


**Figure 13.** Excitation and reaction pathways which occur during low-energy electron irradiation of the NaNO<sub>3</sub> crystal surface and near-surface region. Irradiation-induced pathways are drawn with wavy arrows. The scheme illustrates the primary processes which lead to the production and desorption of nonthermal O and NO fragments and also mechanisms for thermal NO + O<sub>2</sub> desorption. Note the dotted circle implies these processes occur subsurface and under relatively high dose conditions.

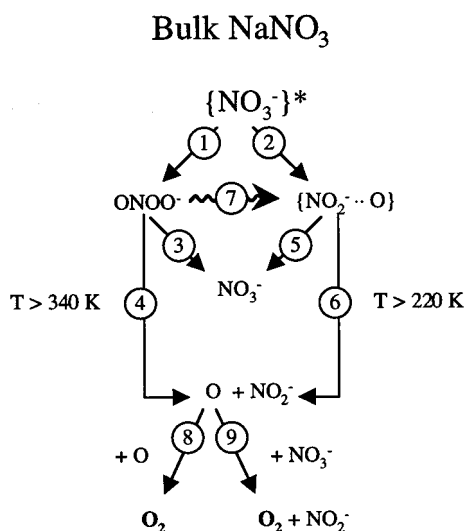


**Figure 14.** Scheme for bulk processes, which occur during electron irradiation of NaNO<sub>3</sub> crystals. Irradiation-induced pathways are drawn with wavy arrows. The scheme shows the cage-limited decay of the  $\{\text{NO}_3^-\}^*$  ions in the bulk of the NaNO<sub>3</sub> and two major reaction pathways for the O<sub>2</sub> post-irradiation TPD, attributed to the P<sub>1</sub> peak at  $\sim 260 \text{ K}$  and P<sub>2</sub> peak at  $\sim 340 \text{ K}$ .

of NaNO<sub>3</sub> crystal surfaces and bulk, respectively. The importance of O atom production via decay of excited nitrate (reaction 3 in Figure 13) has been proposed several times as the initial step in radiation damage of NaNO<sub>3</sub>.<sup>16,29</sup> In the case of PSD using 6.4 eV photons, it was suggested that excited  $\{\text{NO}_3^-\}^*$  is unstable at the surface and dissociation of this complex produces

O and NO as well as O<sup>-</sup> trapped at the surface<sup>16,29</sup> (reactions 3 and 4, Figure 13). The nonthermal O (<sup>3</sup>P<sub>J</sub>) state distribution (Figure 2) and the  $\sim 6 \text{ eV}$  threshold energy (Figure 3) demonstrate that this channel is important in ESD of NaNO<sub>3</sub>.

A second threshold near 10 eV indicates that electrons and holes are also involved in the ESD of NO and O (process 2 in Figure 13). However, the similar electron energy dependence and constant NO/O ratio over the entire energy range studied suggests that electrons and holes recombine rapidly at high temperatures creating  $\{\text{NO}_3^-\}^*$  (reaction 5, Figure 13). This excited-state dissociates to O and NO (reactions 3 and 4, Figure 13). Pulsed irradiation and luminescence experiments<sup>12-14</sup> suggest that recombination occurs on the NO<sub>3</sub><sup>-</sup> site of the lattice between free and trapped carriers; electrons recombine with self-trapped holes (NO<sub>3</sub><sup>-</sup> centers) and/or holes recombine with self-trapped electrons (NO<sub>3</sub><sup>2-</sup> centers).

Typically, irradiation with incident energy  $E_i$  between  $E_g$  and  $\sim 2E_g$  creates one electron-hole pair per photon (particle)<sup>39</sup> and the number of electron-hole pairs produced by the higher energy irradiation increases with energy and can be approximated<sup>39</sup> by  $\sim E_i/2E_g$ . This is consistent with the monotonic increase of the ESD yield with energy above  $2E_g$  (Figure 3).

Electron-hole recombination supplies extra energy to NO<sub>3</sub><sup>-</sup>\* when compared to the  $\pi^* \leftarrow \pi$  excitation. This excess energy leads to the production and desorption of significantly more energetic O and NO products relative to PSD using UV photons.<sup>16</sup> In the ESD case, the effective translational temperatures of the NO (<sup>2</sup>Π)(0,0) and O (<sup>3</sup>P<sub>2</sub>) were  $\sim 1600$  and  $2000 \text{ K}$ , respectively. For PSD, the translational temperatures were  $\sim 1300$  and  $1400 \text{ K}$  for the same states of NO and O, respectively.<sup>16</sup> In ESD, Figures 4 and 5 indicate that a significant part of the recombination energy is also partitioned into NO rotational and vibrational energy and population of the higher J states of the O(<sup>3</sup>P<sub>J</sub>) atoms.

Dissociation of the  $\{\text{NO}_3^-\}^*$  in the bulk of alkali nitrate crystals is suppressed by the cage effect. Thus, the primary process of bulk defect creation is limited by the probability of  $\{\text{NO}_2^- \cdots \text{O}\}$  complex separation<sup>7,22,24</sup> (reaction 6, Figure 14). The reported temperature dependence of NO<sub>2</sub><sup>-</sup> production in irradiated NaNO<sub>3</sub> demonstrates the presence of radiation and radiation thermal<sup>22,23,41,42</sup> components which are characterized by  $0-0.004 \text{ eV}$ <sup>23</sup> and  $\sim 0.12 \text{ eV}$ <sup>22,23</sup> apparent activation energies, respectively. The translational energy of the hot O atoms measured in our experiments peaks at  $\sim 0.17 \text{ eV}$ , which is higher than a 0.12 eV barrier for separation of the  $\{\text{NO}_2^- \cdots \text{O}\}$  complex. O atoms whose energy exceeds the 0.12 eV cage-induced barrier can escape the cage without thermal activation. Hence, the radiation and radiation thermal components associated with the temperature-dependent NO<sub>2</sub><sup>-</sup> yields can be associated with the generation of hot and thermal oxygen atoms during decay of the excited nitrate anions, respectively. The presented data indicates that radiation damage of the surface and bulk of NaNO<sub>3</sub> crystals initially involves the decay of the  $\pi^*$  excited nitrate anion yielding hot O atoms. The next step of this dissociation process yields NO at the surface but not in the bulk.

**B. Delayed Emission: Precursor Formation and Unimolecular Dissociation.** It is important to note that the delayed desorption of NO and O<sub>2</sub> from the irradiated NaNO<sub>3</sub> solids occurs synchronously with identical temperature dependencies and a constant stoichiometric ratio. It seems logical to associate this delayed emission with a common precursor. We suggest surface NO<sub>3</sub> radicals as candidates for the precursor species. Traces of NO observed by several authors<sup>7,43,44</sup> in the bulk of



irradiated alkali nitrates were also attributed to this precursor. The  $^2E'$  excited state of  $\text{NO}_3$  can undergo unimolecular dissociation yielding  $\text{NO}$  ( $^2\Pi$ ) and  $\text{O}_2$  ( $^3\Sigma_g^-, ^1\Delta_g$ ) molecules<sup>45–49</sup> due to vibronic coupling to the  $\text{NO}_3$  ( $^2A_2'$ ) ground state (reaction 9, Figure 13). This excited state is long-lived, dissociating on the time scale of hundreds of microseconds in the gas phase.<sup>45,49</sup> Another possible source of the  $\text{NO}$  and  $\text{O}_2$  synchronous desorption may be the  $\text{N}_2\text{O}_4$  dimer which can be produced via the  $2\text{NO}_2 \leftrightarrow \text{N}_2\text{O}_4 \leftrightarrow 2\text{NO} + \text{O}_2$  reaction sequence. However, two main reasons allow us to rule out this precursor: (i) the dissociation probability of  $\text{N}_2\text{O}_4$  below 300 K is very low and (ii) the production probability of  $\text{N}_2\text{O}_4$  at temperatures above 400 K is also very low.

The  $\text{NO}_3$  radical was detected in irradiated alkali nitrate crystals at 77 K and was assigned as the product of hole autolocalization.<sup>9,10</sup> Its lifetime at 300 K is limited by recombination with electrons and is on the order of  $10^{-7}$  s.<sup>10,12–14</sup> The hole can also be produced without a valence-to-conduction band transition since unoccupied midgap (defect) states, which are correlated with the presence of  $\text{NO}_2^-$ , exist. Time-resolved luminescence measurements indicate that such holes may have much longer lifetimes without conduction band electrons as recombination partners.<sup>50</sup>  $\text{NO}_2^-$  ions are primary products of the photo/radiation-induced decomposition of alkali nitrates, and their concentration can be high.<sup>8,27,51</sup>  $\text{NO}_2^-$  states in  $\text{NaNO}_3$  should lie in the band gap, about 1 eV from the top of the valence band<sup>1</sup> and electron transitions to this state can produce holes and  $\text{NO}_2^{2-}$  centers (reaction 7, Figure 13). This contention is supported by earlier ESR studies of irradiated nitrates.<sup>52–54</sup>

We suggest that the observed  $\text{NO}$  and  $\text{O}_2$  ESD temperature dependence is due to the temperature dependence of  $\text{NO}_2^-$  production. The  $\text{NO}_2^-$  is a source of holes, which migrate to the surface and recombine with  $\text{NO}_3^-$  to produce  $\text{NO}_3^*$  precursors (reaction 8, Figure 13). This proposed mechanism does not need a fundamental ionization event and can successfully explain delayed  $\text{NO}$  and  $\text{O}_2$  emission induced by 5 and 6.4 eV photons.<sup>16,29,33</sup> *The dashed circle in Figure 13 indicates that this channel only becomes significant under high-dose conditions where a sufficient number density of  $\text{NO}_2^-$  defect sites exist.* Note, we do not rule out direct production of surface  $\text{NO}_3^*$  centers via deep valence or shallow core-level ionization events.<sup>28</sup> We suppose that, under the given experimental conditions, the majority of the  $\text{NO}_3^*$  centers will recombine with electrons<sup>10</sup> prior to the slow unimolecular dissociation. The remaining surface  $\text{NO}_3^*$  centers, statistically compensated by the bulk  $\text{NO}_2^{2-}$  defects, should have enough time for dissociation.

$\text{NO}_2$  is a minor  $\text{NaNO}_3$  radiation decomposition product. We can associate the  $\text{NO}_2$  production with surface  $\text{NO}_2^-$  defect trapping of holes, as was shown for the bulk radiolysis.<sup>9,11</sup> Other possible sources of  $\text{NO}_2$  may be attributed to decay of surface  $\text{NO}_3^{2-}$  and/or  $\text{NO}_3$  centers via  $\text{NO}_3^{2-} \rightarrow \text{NO}_2 + \text{O}^{2-}$  and  $\text{NO}_3^* \rightarrow \text{NO}_2 + \text{O}$ , respectively.<sup>45,49</sup>

**C. Post-Irradiation Thermal-Stimulated Desorption and Decomposition of Radiation Induced Defects.** The release of the molecular oxygen during thermal annealing of pre-irradiated crystals is not surprising. Several authors discovered that  $\text{O}_2$  (>98.5%) is liberated from irradiated potassium and sodium nitrate crystals during dissolution, melting, or mechanical crushing.<sup>55–57</sup> However, there were no observations of oxygen escaping the irradiated crystal during thermal annealing below 400 K. In the bulk,  $\text{O}_2$  is the product of O atom recombination (reaction 8, Figure 14) and reactive scattering with the  $\text{NO}_3^-$  anion (reaction 9, Figure 14).<sup>6,7,43,56</sup> The yield of free O atoms

in irradiated crystalline nitrates at temperatures below 200 K is low<sup>14,17,18,20</sup> and may be associated with hot oxygen atoms (see part A of the Discussion) produced during dissociation of  $\{\text{NO}_3^-\}^*$ .

The radiation damage induced by 100 eV electrons is concentrated in the first few nanometers of the crystal. Thus, oxygen molecules should diffuse to the surface and desorb during the thermal annealing of the irradiated crystals. Such thermal activated diffusion of  $\text{O}_2$  molecules is likely responsible for the long monotonic tail of the TPD curve at low irradiation doses (Figure 9). The main potential sources of oxygen production at low irradiation temperature (110 K) are the peroxy-nitrite anion ( $\text{ONOO}^-$ )<sup>14,17,20</sup> and the complex  $\{\text{NO}_2 \cdots \text{O}\}$ .<sup>21</sup> The  $\text{ONOO}^-$  is stable up to  $\sim 360$  K in  $\text{KNO}_3$  which is close to the position of the main TPD maximum ( $P_2$ ) in Figure 9. It can rearrange to form nitrate (reaction 3, Figure 14) or decompose to form nitrite and O atoms (reaction 4, Figure 14).<sup>14,17,20</sup> The bound  $\{\text{NO}_2 \cdots \text{O}\}$  complex starts releasing O atoms at  $> 220$  K<sup>14</sup> (reaction 6, Figure 13) which is close to the position of the first maximum ( $P_1$ ) in Figure 9.

The dose dependence of the high-temperature TPD peak ( $P_2$ ) has a clear tendency toward saturation (Figure 10). This saturation feature is typical for accumulation of peroxy-nitrite<sup>17,20</sup> and is caused by radiation-induced decomposition yielding nitrate and  $\{\text{NO}_2 \cdots \text{O}\}$  complexes (reactions 7, 5, and 6, Figure 14).<sup>17,20</sup> Thus, with higher doses, we shall expect an increasing contribution of the  $\{\text{NO}_2 \cdots \text{O}\}$  complex to the total oxygen production due to reactions 6–9 in Figure 14. The TPD peak ( $P_1$ ) at  $\sim 260$  K (Figure 9) perfectly fits this feature; it has a “delayed” dose dependence (Figure 10), and the temperature of the leading desorption edge is very close to the onset temperature ( $\sim 220$  K) for thermal decomposition of  $\{\text{NO}_2 \cdots \text{O}\}$ .<sup>14</sup> Therefore, thermal annealing of irradiated  $\text{NaNO}_3$  crystals, which activates the decay of bulk radiation defects, produces oxygen which then diffuses to the surface.

## V. Conclusions

Electron beam induced damage of  $\text{NaNO}_3$  single crystals initially involves destruction of the nitrate group and production of O ( $^3P_j$ ) and  $\text{NO}$  ( $^2\Pi$ ) fragments with nonthermal energy distributions. This channel is dominated by the decay of  $\{\text{NO}_3^-\}^*$ . At higher electron fluences, thermalized  $\text{NO}$ ,  $\text{O}_2$ , and  $\text{NO}_2$  are also produced and released, though the  $\text{NO}_2$  is a minor product. Yields of thermalized  $\text{NO}$  and  $\text{O}_2$  exhibit similar temperature dependencies. We suggest that the formation and desorption of thermalized  $\text{NO}$  and  $\text{O}_2$  involve  $\text{NO}_2^-$  defect states and unimolecular dissociation of  $\text{NO}_3^*$ .  $\text{O}_2$  gas is also released during heating of  $\text{NaNO}_3$  irradiated at 110 K. We associate the post-irradiation TPD of  $\text{O}_2$  with reactions involving O atoms released during thermal decomposition of  $\{\text{NO}_2 \cdots \text{O}\}$  and  $\text{ONOO}^-$ . The SEEM image shows damage features, and the AES spectra indicate that the irradiated region is depleted in both nitrogen and oxygen relative to Na. The elemental composition shows  $\text{Na}_2\text{O}$  as a final product of the  $\text{NaNO}_3$  radiation decomposition. The 100 eV electron-induced damage cross section is at least  $\sim 10^{-16}$  cm<sup>2</sup>. This damage involves the production of species, such as  $\text{NO}$ ,  $\text{O}_2$ , O, and  $\text{O}^-$  which can contribute to oxidative aging and flammable gas production in “mixed” (radioactive/chemical) wastes.

**Acknowledgment.** The SEEM, TPD, and AES work was supported by the U. S. Department of Energy, Environmental Management Science Program, Project 54646. The REMPI studies were supported by the U. S. Department of Energy,



Office of Basic Energy Sciences. All work was performed at the W. R. Wiley, Environmental Molecular Sciences Laboratory, a national scientific user facility sponsored by the Department of Energy's Office of Biological and Environmental Research and located at Pacific Northwest National Laboratory (PNNL). PNNL is operated for the U. S. Department of Energy by Battelle Memorial Institute under Contract DE-AC06-76RLO 1830. N.G.P. and K.K. were supported by the Associated Western Universities, Inc. under Grant DE-FG06-92RL-12451. E. Paparazzo and T. M. Orlando also thank the North Atlantic Treaty Organization (NATO) for a Collaborative Research Grant (CRG 972114) which provided travel funds. T.M.O. also thanks D. Meisel of the University of Notre Dame, N. Zema of the CNR (Rome, Italy), and M. Piacentini of the University of Rome (Italy) for useful discussions.

## References and Notes

- (1) Yamashita, H.; Kato, R. *J. Phys. Soc. Jpn.* **1970**, *29*, 1557.
- (2) Yamashita, H. *J. Phys. Soc. Jpn.* **1972**, *33*, 1407.
- (3) Laux, J. M.; Fister, T. F.; Finlayson-Pitts, B. J.; Hemminger, J. C. *J. Phys. Chem.* **1996**, *100*, 19891.
- (4) Ghosal, S.; Hemminger, J. C. *J. Phys. Chem. A* **1999**, *103*, 4777.
- (5) Hanford Seeks Short and Long-Term Solutions to Its Legacy of Wastes. *Phys. Today* **1992**, March.
- (6) Johnson, E. R. *The Radiation-Induced Decomposition of Inorganic Molecular Ions*; Gordon and Breach: New York, 1970.
- (7) Cunningham, J. Fragments in Irradiated Ionis Solids. In *Radical Ions*; Kaiser, E. T., Kevan, L., Eds.; Interscience: New York, 1968; p 475.
- (8) Sasaki, T.; Williams, R. S.; Wong, J. S.; Shirley, D. A. *J. Chem. Phys.* **1978**, *68*, 2718.
- (9) Nevostruev, V. A.; Pak, V. K.; Bannov, S. I. *Russ. J. Phys. Chem.* **1991**, *65*, 799.
- (10) Nevostruev, V. A.; Pak, V. K.; Bannov, S. I. *High Energy Chem.* **1990**, *24*, 24.
- (11) Zeldes, H.; Livingston, R. J. *J. Chem. Phys.* **1962**, *37*, 3017.
- (12) Dolganov, V. S. *High Energy Chem.* **1989**, *23*, 295.
- (13) Dolganov, V. S. *High Energy Chem.* **1993**, *27*, 52.
- (14) Safonov, Y. N. Pulse Radiolysis of Oxyanion Crystals. Doctoral Thesis, Institute of Technology, St. Petersburg, Russia, 1996.
- (15) Bannov, S. I.; Pak, V. K.; Nevostruev, V. A.; Khisamov, B. A. *High Energy Chem.* **1991**, *25*, 76.
- (16) Knutsen, K.; Orlando, T. M. *Phys. Rev. B* **1997**, *55*, 13246.
- (17) Plumb, R. C.; Edwards, J. O. *J. Phys. Chem.* **1992**, *96*, 3245.
- (18) Yurmazova, T. A.; Koval, L. N.; Serikov, L. V. *High Energy Chem.* **1983**, *17*, 151.
- (19) Nevostruev, V. A.; Miklin, M. B. *High Energy Chem.* **1987**, *21*, 126.
- (20) Yurmazova, T. A. Role of pernitrite in the nitrate ion transformations under irradiation. Doctoral Thesis, Institute of Technology, St. Petersburg, Russia, 1988.
- (21) Bannov, S. I.; Khisamov, B. A. *High Energy Chem.* **1997**, *31*, 196.
- (22) Cunningham, J. J. *J. Phys. Chem.* **1961**, *65*, 628.
- (23) Iirgena, T. S.; Bugaenko, L. T.; Tiliks, Y. E. *High Energy Chem.* **1981**, *15*, 328.
- (24) Cunningham, J.; Steele, L. R. *Phys. Rev. Lett.* **1962**, *9*, 47.
- (25) Hochanadel, C. J.; Davis, T. W. *J. Chem. Phys.* **1957**, *27*, 333.
- (26) Yurmazova, T. A.; Koval, L. N.; Serikov, L. V. *High Energy Chem.* **1983**, *17*, 120.
- (27) Shin, J.-J.; Langford, S. C.; Dickinson, J. T.; Wu, Y. *Nucl. Instrum. Methods Phys. Res. B* **1995**, *103*, 284.
- (28) Knutsen, K.; Orlando, T. M. *Surf. Sci.* **1996**, *348*, 143.
- (29) Knutsen, K.; Orlando, T. M. *Appl. Surf. Sci.* **1998**, *127-129*, 1.
- (30) Hess, W. P.; German, K. A. H.; Bradley, R. A.; McCarthy, M. I. *Appl. Surf. Sci.* **1996**, *96-98*, 321.
- (31) Dickinson, J. T.; Shin, J. J.; Langford, S. C. *Appl. Surf. Sci.* **1996**, *96-98*, 326.
- (32) Bradley, R. A.; Lanzendorf, E.; McCarthy, M. I.; Orlando, T. M.; Hess, W. P. *J. Phys. Chem.* **1995**, *99*, 11715.
- (33) Webb, R. L.; Langford, S. C.; Dickinson, J. T. *Nucl. Instrum. Methods Phys. Res., Sect. B* **1995**, *103*, 297.
- (34) Shin, J. J.; Kim, M.-W.; Dickinson, J. T. *J. Appl. Phys.* **1996**, *80*, 7065.
- (35) Piper, L. G.; Cowles, L. M. *J. Chem. Phys.* **1986**, *85*, 2419.
- (36) Bamford, D. J.; Jusinski, L. E.; Bischel, W. K. *Phys. Rev. A* **1986**, *34*, 185.
- (37) Childs, K. D. *Handbook of Auger Electron Spectroscopy*; Physical Electronics: Eden Prairie, MN, 1995.
- (38) Stechel, E. B.; Burns, A. R.; Jennison, D. R. *Surf. Sci.* **1995**, *340*, 71.
- (39) Itoh, N. *Radiat. Eff.* **1998**, *146*, 1.
- (40) Tanuma, S.; Powell, C. J.; Penn, D. R. *J. Vac. Sci. Technol.* **1990**, *A8*, 2213.
- (41) Logan, S. R.; Moore, W. J. *J. Phys. Chem.* **1963**, *67*, 1042.
- (42) Cunningham, J.; Heal, H. G. *Trans. Faraday Soc.* **1958**, *54*, 1355.
- (43) Zakharov, Y. A.; Nevostruev, V. A. *Russ. Chem. Rev.* **1968**, *37*, 61.
- (44) Pogge, H. B.; Jones, F. T. *J. Phys. Chem.* **1970**, *74*, 1700.
- (45) Mikhaylichenko, K.; Riehn, C.; Valachovic, L.; Sanov, A.; Wittig, C. *J. Chem. Phys.* **1996**, *105*, 6807.
- (46) Davis, H. F.; Kim, B.; Johnston, H. S.; Lee, Y. T. *J. Phys. Chem.* **1993**, *97*, 2172.
- (47) Weaver, A.; Arnold, D. W.; Bradforth, S. E.; Neumark, D. M. *J. Chem. Phys.* **1991**, *94*, 1740.
- (48) Mayer, M.; Gederbaum, L. S.; Köppel, H. *J. Chem. Phys.* **1994**, *100*, 899.
- (49) Nelson, H. H.; Pasternack, L.; McDonald, J. R. *J. Chem. Phys.* **1983**, *79*, 4279.
- (50) Petrik, N. G.; Taylor, D. P.; Orlando, T. M. *J. Appl. Phys.* **1999**, *85*, 6770.
- (51) Aduru, S.; Contarini, S.; Rabalais, J. W. *J. Phys. Chem.* **1986**, *90*, 1683.
- (52) Tagaya, K. *Jpn. J. Appl. Phys.* **1986**, *25*, 469.
- (53) Atkins, P. W.; Symons, M. C. R. *J. Chem. Soc.* **1962**, 4794.
- (54) Cunningham, J. J. *J. Phys. Chem.* **1962**, *66*, 779.
- (55) Allen, A. O.; Chromly, J. H. *J. Chem. Phys.* **1947**, *15*, 208.
- (56) Hennig, G.; Lees, R.; Matheson, M. S. *J. Chem. Phys.* **1953**, *21*, 664.
- (57) Johnson, E. R.; Forten, J. *Discuss Faraday Soc.* **1961**, *31*, 238.